JOURNAL OF AIRCRAFT
Vol. 47, No. 1, January–February 2010

Computation of Unsteady Low Reynolds Number Free-Flight Aerodynamics of Flapping Wings

Dominic D. J. Chandar* and M. Damodaran†
Nanyang Technological University, Singapore 639798, Republic of Singapore

DOI: 10.2514/1.44456

The observation that thrust is produced when a wing flaps above a particular reduced frequency at low Reynolds numbers has been associated with the formation of a reverse Kármán vortex street. Through experiments, numerical computations, and analytical methods, scientists have been able to explain thrust generation in birds and insects. This has increased the interest in the development of micro aerial vehicles. There is, however, a paucity of experimental or computational studies that explain the basic mechanism of thrust generation from the viewpoint of the surrounding vortical structures and the effect of these vortices on free flight when the wing is accelerating in the direction of thrust. In the present work, three-dimensional free-flight computations are carried out on flapping wings that have rectangular planforms composed of NACA 0012 and an elliptical airfoil section, respectively, to demonstrate that thrust is generated as a result of vortex asymmetry. Based on the computed vortex dynamics, it is also shown that the relative convection rates of positive and negative vorticity are a key parameter involved in thrust generation. Numerical computations are performed using the unsteady three-dimensional Navier–Stokes solver composite grid incompressible Navier–Stokes, which is based on the Overture framework for overlapping grids. Comparative analysis with existing experimental/computational data is also presented.

Nomenclature

C_p	=	power input coefficient
C_T	=	thrust coefficient ($= -C_D$, drag coefficient)
c	=	chord length or mean aerodynamic chord
$\boldsymbol{F}$	=	body force
$\boldsymbol{F}_{\mathrm{A}}$	=	aerodynamic forces (lift, drag)
f	=	oscillation frequency
H	=	span of the computational domain along the Y axis
h_0	=	plunge amplitude scaled by chord
k	=	reduced frequency, $=\pi fc/U_\infty$
M	=	mass of the airfoil/wing
p	=	pressure
Re	=	Reynolds number, $=U_S c/\upsilon$
r'	=	arbitrary point on a rigid body
S	=	wingspan
St	=	Strouhal number, $=kh_0$
U_S	=	velocity scale
$\boldsymbol{u}$	=	velocity field (u, v, w)
W	=	span of the computational domain along the X axis
$\boldsymbol{x}_{\mathrm{cm}}$	=	center of mass
Δt	=	time step
α	=	first moment of vorticity
θ_0	=	amplitude of rotation
ρ_b	=	density of airfoil/wing
ρ_f	=	density of the fluid
υ	=	kinematic viscosity
ω	=	vorticity

Presented as Paper 420 at the AIAA 46th AIAA Aerospace Sciences Meeting, Reno, NV, 5–8 January 2008; received 19 March 2009; accepted for publication 31 July 2009.

*Graduate Student, Division of Thermal and Fluids Engineering, School of Mechanical and Aerospace Engineering, 50 Nanyang Avenue; domi0002@ntu.edu.sg. Student Member AIAA.

†Associate Professor, Division of Thermal and Fluids Engineering, School of Mechanical and Aerospace Engineering, 50 Nanyang Avenue; mdamodaran@ntu.edu.sg. Associate Fellow AIAA.

I. Introduction

IT IS well known that the motion of insects and birds are governed by unsteady aerodynamic forces that are created by rapid wing movements. Thrust generation in flapping airfoils at low Reynolds numbers is usually associated with the formation of a reverse Kármán vortex street [1]. The standard approach that has been adopted by the scientific community is to study the aerodynamic characteristics of flapping wings with a fixed freestream velocity. In this approach, a uniform stream of fluid flows past a plunging/pitching wing and the effect of kinematics, reduced frequency, Strouhal number, and Reynolds number on the aerodynamic characteristics are analyzed [2–6]. Based on the observed or computed thrust/lift/power coefficients, a suitable combination of nondimensional parameters could be identified as a best possible set that maximizes either thrust or propulsive efficiency. An alternative approach that is adopted is to set the body free to move under the action of aerodynamic forces with no incoming freestream. In this case, the body accelerates from the state of rest to the state of motion. In an experiment by Vandenberghe et al. [7], the problem of forward flight has been discussed in detail with more emphasis to the passive motion of the wing undergoing forced plunge oscillations. The transition between the state of rest and free flight is shown to take place at a critical reduced frequency. Alben and Shelly [8] verified the observation of Vandenberghe et al. [7] through two-dimensional numerical computations. Beal et al. [9] performed experiments on a dead trout placed downstream of a cylinder and demonstrated that under certain conditions, it can extract energy from the wake of the cylinder and propel itself upstream.

Based on the observation by Lai and Platzer [10], prior work conducted by the present authors [11] showed that airfoils having sharper trailing edges traveled faster than their blunt counterparts. However, the physical reasoning behind this behavior was not discussed in detail. In both the previously described approaches, the manner in which thrust is generated may or may not be the same. For example, when there is an incoming freestream, Anderson et al. [6] showed that for high efficiency the leading-edge vortex is convected downstream and interacts with the trailing-edge vortex to produce a reverse Kármán vortex street. However, when there is no incoming freestream the vortices generated from the leading edge of the wing are not convected downstream and hence, the reverse Kármán vortex street is not visible although thrust is being generated. Based on these observations, there is a need to resort to nonconventional ways to analyze the origin of these forces. The approach that is used is based on the analysis of Wu [12], who derived expressions for the

aerodynamic forces acting on a solid body as a function of vorticity moments and inertial forces. A brief analysis to explain lift generation in tiny insects based on this theory can be found in Miller and Peskin [13]. The main objectives of the paper are thus to 1) demonstrate the problem of free-flight in three dimensions, 2) investigate the effect of kinematics on thrust generation and forward flight, 3) study the effect of leading- edge–trailing-edge asymmetry on thrust generation, and 4) correlate thrust with the vorticity convection rates. In the course of the investigation, it will be seen that the interplay between positive and negative vorticity is a key feature that determines the level of thrust generated. Numerical computations are performed on moving and overlapping meshes using the unsteady composite grid incompressible Navier–Stokes solver (cgins) [14], which is based upon the Overture [15] framework. The numerical method, followed by validation and accuracy studies, is discussed in the sections to follow.

II. Governing Equations and Numerical Method

The governing equations are the unsteady incompressible Navier–Stokes equations given by

$$\mathbf{u}_t + (\mathbf{u} \bullet \nabla)\mathbf{u} + \frac{\nabla p}{\rho} = \upsilon \Delta \mathbf{u} + \mathbf{F} \tag{1}$$

$$\nabla . \mathbf{u} = 0 \tag{2}$$

The numerical method and convergence studies are well described in Henshaw [14], Brown et al. [15], Chesshire and Henshaw [16], and Chandar and Damodaran [11]. However, a brief description of the method is provided here. These equations are discretized in space on a system of overlapping meshes (see Fig. 1). Each of those meshes is a mapping from the physical domain with coordinates $\boldsymbol{x}$ to the computational domain with coordinates $\boldsymbol{r}$. This mapping is defined in Chesshire and Henshaw [16] as $\boldsymbol{x} = \boldsymbol{G}(\boldsymbol{r})$. For a mesh that is moving with the body (rigidly), this mapping is a function of time given by $\boldsymbol{x} = \boldsymbol{G}(\boldsymbol{r}, t)$, $t = \tau$. Hence, the momentum Eq. (1) in the reference frame moving with the mesh is transformed to

$$\frac{\partial \mathbf{u}}{\partial \tau} + \left[(u_{\mathbf{i}} - \dot{G}_{\mathbf{i}})\left(\frac{\partial r_{\mathbf{j}}}{\partial x_{\mathbf{i}}}\right)\frac{\partial}{\partial r_{\mathbf{j}}}\right]\mathbf{u} + \frac{1}{\rho}\left(\frac{\partial r_{\mathbf{j}}}{\partial x_{\mathbf{i}}}\right)\frac{\partial p}{\partial r_{\mathbf{j}}} = \upsilon \frac{\partial}{\partial r_m}\left(\frac{\partial r_j}{\partial x_{\mathbf{q}}}\frac{\partial u_{\mathbf{i}}}{\partial r_j}\right)\frac{\partial r_m}{\partial x_q} + \mathbf{F} \tag{3}$$

and the pressure is determined from the incompressibility constraint $\nabla . \mathbf{u} = 0$ as

$$\tilde{\Delta} p + \rho \sum_i \tilde{\nabla} u_{\mathbf{i}} \bullet \frac{\partial \mathbf{u}}{\partial x_i} = 0 \tag{4}$$

The modified operators $\tilde{\nabla}$ and $\tilde{\Delta}$ are defined as

$$\tilde{\nabla}_k = \frac{\partial r_j}{\partial x_k}\frac{\partial}{\partial r_j}, \qquad \tilde{\Delta} = \frac{\partial}{\partial r_m}\left(\frac{\partial r_j}{\partial x_{\mathbf{q}}}\frac{\partial}{\partial r_j}\right)\frac{\partial r_m}{\partial x_q} \tag{5}$$

The overlapping meshes are generated using the grid generator Ogen [17], which has its basis on the composite grid (CMPGRD) algorithm by Chesshire and Henshaw [16]. A set of mappings are generated corresponding to each component meshes, and each mapping maps the unit square to the physical domain. The solutions in the region of overlap are interpolated at appropriate interpolation points in the computational domain using a Lagrange interpolation formula of the form $u_{ij} = \alpha \cdot u_{\mathrm{In}}$ where α, $\boldsymbol{u}_{\mathrm{In}}$ are second-order tensors that denote the interpolation weights and solutions from which the interpolation should be performed. Figure 1a shows a set of overlapping structured meshes around a NACA 0012 cross section wing generated using a hyperbolic grid generation algorithm. The volume meshes surrounding the wing (A, B, and C) are curvilinear, structured, and overlap in a finite region. An orthographic patch or a mapping (A, B) is used to mesh the wing tips. Details can be found in Henshaw [18]. These meshes then overlap with a background Cartesian mesh as shown in Fig. 1b.

Second-order central differences are used for discretizing the convection terms in the momentum Eq. (3). The discretized equations are solved using a fractional step method that is second-order accurate for both pressure and velocity with boundary conditions $B(\mathbf{u}, p) = 0$, $\nabla \bullet \mathbf{u} = 0$ and initial conditions $\mathbf{u}(\boldsymbol{x}, 0) = \mathbf{u_0}(\boldsymbol{x})$. The boundary condition for pressure is obtained by taking the dot product of the momentum equation with the normal. For moving boundaries, the boundary condition also includes the boundary acceleration given by

$$\frac{\partial p}{\partial n} = n \cdot (-\ddot{G} - \upsilon \tilde{\nabla} \times \tilde{\nabla} \times \mathbf{u}) \tag{6}$$

Semi-implicit time stepping using a multistep predictor corrector method is used for advancing the solution in time. The discretization results in a set of linear equations that are solved using the portable extensible toolkit for scientific computing (PETSC) [19]. PETSC [19] uses a variety of direct and iterative algorithms for sparse matrix computations. For all computations, the biconjugate gradient stabilized method [20] is used. The pressure equation [Eq. (4)] is also solved in a similar way.

A. Rigid Body Dynamics

Because the wing is considered as a rigid body moving under the action of aerodynamic forces $\mathbf{F_A}$, its position $\boldsymbol{x}_{\mathbf{cm}}$, velocity, and acceleration have to be determined at each time instant t. This information is obtained by solving the equations of motion for a rigid body,

$$M \frac{d^2 \boldsymbol{x}_{\mathbf{cm}}}{dt^2} = \mathbf{F_A} \tag{7}$$

where $\boldsymbol{x}_{\mathbf{cm}}$ is the position of the center of mass, and $\mathbf{F_A}$ are the aerodynamic forces acting on the center of mass and are obtained as

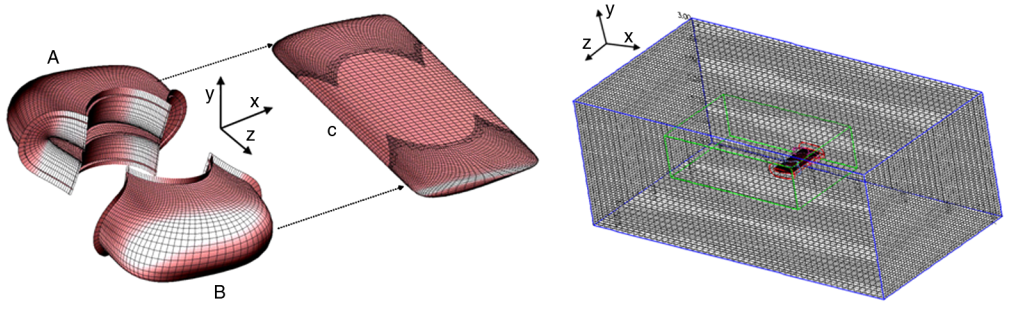

a) **b)**

Fig. 1 The system of overlapping meshes a) surrounding the wing, and b) the complete set of overlapping meshes.

$\mathbf{F_A} = \int_{d\Omega} pn_i - n_k\tau_{ki}\mathrm{d}S$. The position of the center of mass can then be obtained by integrating Eq. (7). At each time instant t, the acceleration is updated from the forces and is used in Eq. (6) for the solution of pressure. The overall solution procedure is outlined in Sec. II.C.

B. Computational Domain: Initial and Boundary Conditions

The computational domain in Fig. 2 consists of a collection of meshes, which include three volume meshes surrounding the wing and two Cartesian meshes (the inner and outer cube). The inner cube has all its boundaries as interpolation points whereas the outer cube is assumed to be a physical boundary that consists of slip walls (P-R-R 1-P 1-P, Q-S-S 1-Q 1-Q, Q-P-P 1-Q 1-Q, and S-R-R 1-S 1-S), inflow (P-Q-S-R-P) and outflow boundaries (P 1-Q 1-S 1-R 1-P 1). For clarity, the slip walls identified by Q-P-P 1-Q 1-Q and S-R-R 1-S 1-S are not labeled in Fig. 2. The boundary conditions for the momentum Eq. (3) are summarized in Table 1. The extent of the boundary as described in Fig. 2 is arrived at, based on the analysis in Sec III.

For validation cases that involve an inflow with a finite freestream velocity, the unsteady computation is initialized with the corresponding steady solution whereas for cases with no incoming freestream, the velocity is set to zero everywhere and the initial pressure is computed from the Poisson Eq. (4).

C. Overall Solution Procedure

The solver cgins [14] uses a multistep predictor, corrector algorithm to integrate Eq. (7). This method is outlined in detail in Henshaw and Schwendeman [21]. Starting with the momentum equation Eq. (3), an implicit predictor step is applied for the solution of the predicted velocity ($\mathbf{U^p}$). This results in a set of linear equations of the form

$$\upsilon\Delta\mathbf{u}^p - \frac{2}{\Delta t}\mathbf{u}^p = 3(\mathbf{u}\bullet\nabla\mathbf{u})^n - (\mathbf{u}\bullet\nabla\mathbf{u})^{n-1} + 3\nabla p^n - \nabla p^{n-1} - \frac{2}{\Delta t}\mathbf{u}^n - \upsilon\Delta\mathbf{u}^n \tag{8}$$

At this stage, the forces $\mathbf{F_A}$ are determined and the predictor step for the rigid body equations is called. The predicted linear velocities and displacements are calculated using a centered leap-frog scheme [21]

$$\left(\frac{\mathrm{d}\mathbf{x}_{\mathrm{cm}}}{\mathrm{d}t}\right)^p = \left(\frac{\mathrm{d}\mathbf{x}_{\mathrm{cm}}}{\mathrm{d}t}\right)^{n-1} + 2\Delta t\left(\frac{F_A}{M}\right)^n \tag{9}$$

$$\mathbf{x}_{\mathrm{cm}}^{\,p} = 2\mathbf{x}_{\mathrm{cm}}^n - \mathbf{x}_{\mathrm{cm}}^{n-1} + \Delta t^2\left(\frac{F_A}{M}\right)^n \tag{10}$$

The boundary acceleration is then computed at this intermediate step. Using this information, the pressure equation is solved as

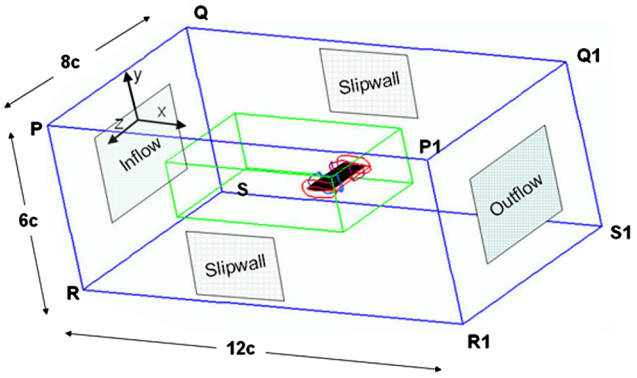

Fig. 2 Computational domain and boundary conditions.

$$\Delta p^p = -\tilde{\nabla}\bullet(\mathbf{u}\bullet\tilde{\nabla}\mathbf{u})^p$$
$$\frac{\partial p}{\partial n} \longleftrightarrow d\Omega = n\bullet(-\ddot{G} - \upsilon\tilde{\nabla}\times\tilde{\nabla}\times\mathbf{u})^p \tag{11}$$

The corrector step is executed using a trapezoidal rule [21] as follows:

$$\upsilon\Delta\mathbf{u}^{n+1} - \frac{2}{\Delta t}\mathbf{u}^{n+1} = (\mathbf{u}\bullet\nabla\mathbf{u})^p + (\mathbf{u}\bullet\nabla\mathbf{u})^n + \nabla p^p + \nabla p^n - \frac{2}{\Delta t}\mathbf{u}^n - \upsilon\Delta\mathbf{u}^n \tag{12}$$

$$\left(\frac{\mathrm{d}\mathbf{x}_{\mathrm{cm}}}{\mathrm{d}t}\right)^{n+1} = \left(\frac{\mathrm{d}\mathbf{x}_{\mathrm{cm}}}{\mathrm{d}t}\right)^n + \frac{\Delta t}{2}\left(\frac{F_A^n}{M} + \frac{F_A^p}{M}\right) \tag{13}$$

$$\mathbf{x}_{\mathrm{cm}}^{\,n+1} = \mathbf{x}_{\mathrm{cm}}^n + \frac{\Delta t}{2}\left(\frac{\mathrm{d}\mathbf{x}_{\mathrm{cm}}^n}{dt} + \frac{\mathrm{d}\mathbf{x}_{\mathrm{cm}}^p}{\mathrm{d}t}\right) \tag{14}$$

The boundary acceleration is computed once again and the pressure equation is solved to determine the updated value at time t^{n+1}.

D. Nondimensional Quantities

The relevant nondimensional quantities are the Reynolds number

$$Re = \frac{U_S c}{\nu}$$

reduced frequency

$$k = \frac{\pi f c}{U_S}$$

and Strouhal number $St = kh_0$. Here U_S is a suitable velocity scale chosen appropriately. When there is an incoming freestream with velocity U_∞ at the inflow boundary, $U_S = U_\infty$. However, when the wing flaps in zero freestream conditions, the maximum translational velocity is taken as the velocity scale. When the wing flaps about the

Table 1 Description of boundary condition types for different regions in the computational domain

Boundary condition type	Region	Boundary condition
Wall (no slip)	Wing surface	$u = 0, \nabla.u = 0, \frac{\partial p}{\partial n} = n\cdot(-\ddot{G} - \upsilon\nabla\times\nabla\times u)$
Slip wall	P-R-R1-P1-P	$n.u = 0, \frac{\partial}{\partial n}(t_m\cdot u) = 0, \nabla.u = 0$
	Q-S-S1-Q1-Q	
	Q-P-P1-Q1-Q	
	S-R-R1-S1-S	
Inflow	P-Q-S-R-P	$u = u_s$ (velocity specified), $\frac{\partial p}{\partial n} = 0$
Outflow	P1-Q1-S1-R1-P1	Extrapolate u, $\frac{\partial p}{\partial n} = 0$

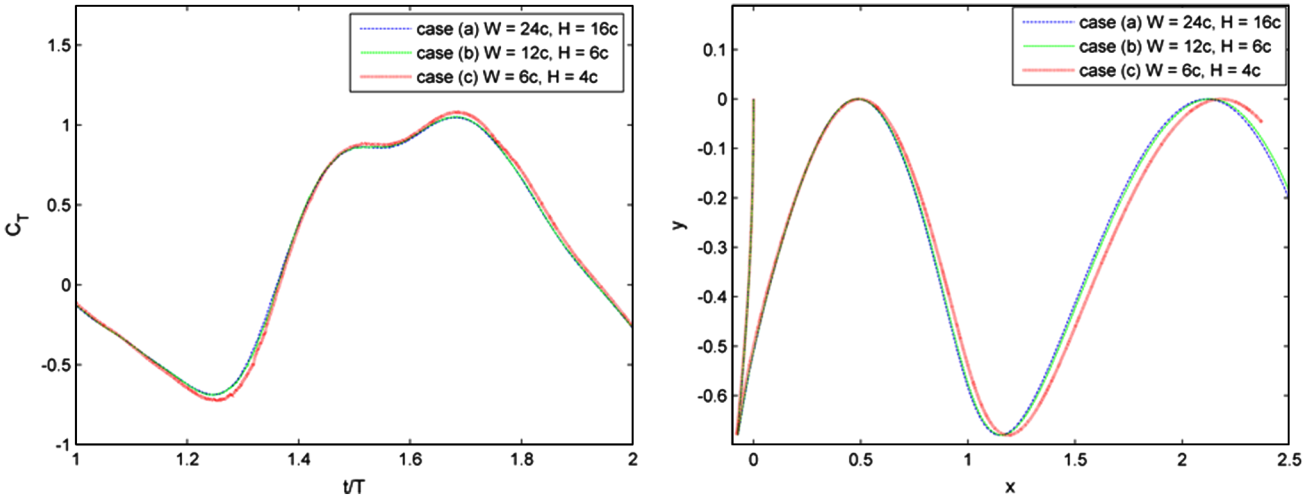

a) b)

Fig. 3 Effect of outer boundary distance on a) thrust coefficient, and b) trajectory.

X axis, according to the notation in Fig. 2, the velocity scale $U_S = 2\pi f\theta_0 S$ and $h_0 = S\sin\theta_0/c$, where θ_0 is the flap angle amplitude and S is the span. The corresponding reduced frequency and Strouhal number are given by

$$k = \frac{c}{2\theta_0 S}$$

$$St = \frac{1}{2}\frac{\sin\theta_0}{\theta_0}$$

respectively. For flapping about the Z axis as described in Fig. 2, the velocity scale $U_S = \pi f\theta_0 c$ and

$$h_0 = \frac{1}{2}\sin\theta_0$$

The corresponding reduced frequency and Strouhal number are given by

$$k = \frac{1}{\theta_0}$$

$$St = \frac{1}{2}\frac{\sin\theta_0}{\theta_0}$$

III. Convergence and Validation

Convergence and validation studies have been reported by the present authors in an earlier paper [11]. No turbulence models have been used either earlier [11] or in the present work at low Reynolds number computations. Presently, comparisons are made for a plunging NACA 0012 cross section wing having aspect ratios 3 and 4 with existing experimental [22] and numerical work [23]. Also mentioned is a comparison with the linear theory of Garrick [24] and the panel code of Young [23]. Apart from correlating the present results with available data, the effect of outer boundary location on the trajectory of a plunging and pitching airfoil is also discussed.

A. Effect of the Outer Boundary on Aerodynamic Characteristics

This assessment is carried out to study the effect of the far-field outer boundary location on the computed aerodynamic characteristics and trajectories of a plunging and pitching 10% thick elliptical cross section airfoil. Three different extents of the outer boundary locations are considered. The width W and height H of the computational domain for these cases are given by 1) $W = 24c$, $H = 16c$, 2) $W = 12c$, $H = 6c$, and 3) $W = 6c$, $H = 4c$ where c is the airfoil chord. The mesh density is maintained the same in all cases and the minimum mesh spacing from the wall is $\mathcal{O}(10^{-4})$. An airfoil having a density $\rho_b = 10\rho_f$ undergoes a combined plunge and pitch oscillation analogous to a flapping wing as described in Sec. IV. The plunge and pitch are governed by the expressions $h = -h_0(1-\cos 2\pi ft)$, $\theta_i = \theta_0(1-\cos 2\pi ft)$, respectively, with $h_0 = 0.34c$, $\theta_0 = 10$ deg, $k = 1.47$, $St = 0.5$, and $Re = 320$. The reduced frequency k, Strouhal number St, and Reynolds number Re have been calculated based on the velocity scale $U_S = 2\pi f h_0$. From the aerodynamic forces, the position of the center of mass is then obtained by integrating Newton's second law for a rigid body [Eq. (7)]. Figure 3a shows the variation of the thrust coefficient C_T for the second cycle for the three cases. Computations show that these forces are either overestimated or underestimated on a smaller domain. The forces corresponding to case b do not differ much from that of case a (very large domain); hence, for three-dimensional computations the span of the outer boundary along X and Y axes is decided based on this fact. The computed trajectory (coordinates of the center of mass) corresponding to these three cases are shown in Fig. 3b. It can be seen that the trajectory corresponding to case c has a larger wavelength compared with that of case a and case b. This shows that on smaller domains, numerical errors will cause the airfoil to travel slower.

B. NACA 0012 Cross Section Wing Plunging at $Re = 10,000$

The test case of a plunging airfoil/wing has been studied by numerous authors through numerical computation and experiments. A compilation of these for a wide range of Reynolds numbers can be found in Ashraf et al. [25]. For the current test case, following the lines of Heathcote et al. [22], a NACA 0012 cross section wing having a rectangular planform with an aspect ratio of 4 is considered. Overlapping grids are generated surrounding the wing as in Fig. 1. A grid refinement study was initially performed and the solutions were considered to be grid independent at this Reynolds number for the grid size mentioned in Table 2. A sinusoidal displacement $h = -h_0(1-\cos 2\pi ft)$ with $h_0 = 0.175c$ is prescribed for the wing.

Table 2 Distribution of points for different grids with reference to Fig. 1

Grid	Number of points (chordwise × spanwise × normal)
Outer cube	51 × 51 × 51
Inner cube	180 × 80 × 90
Wing (C)	172 × 91 × 43
Wing tip (A)	172 × 61 × 43
Wing tip (B)	172 × 61 × 43

Solutions are computed for different reduced frequencies, $k = 0.5$, 1.0, 1.82, 2.5, 3.5, and 4.0 for five cycles of plunging with a time step of $\Delta t = 0.001$. The time-averaged thrust coefficient

$$\bar{C}_T = \frac{2\bar{F}}{\rho U_S^2 Sc}$$

power input coefficient $\bar{C}_p = \frac{2\overline{F_y \dot{h}}}{\rho U_S^3 Sc}$, and propulsive efficiency $\eta = \frac{\bar{C}_T}{\bar{C}_p}$ are then computed for each reduced frequency.

Figures 4a–4c depict the variation of thrust coefficient, power input coefficient, and propulsive efficiency as a function of reduced frequency. An alternative set of computations were performed with an aspect ratio = 3 at $Re = 10000$ and $k = 1.82$. Figure 5 shows a comparison of the thrust coefficient over two cycles of plunging with the experimental results of Heathcote et al. [22]. A close agreement is obtained with existing computational/experimental data indicating that the solutions are computed to a reasonable level of accuracy.

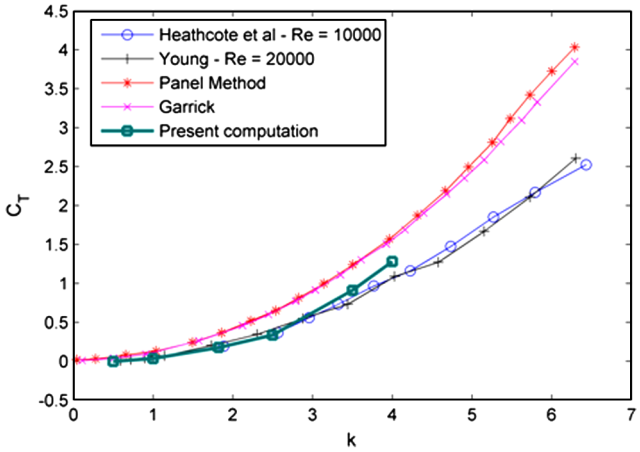

a) Thrust coefficient

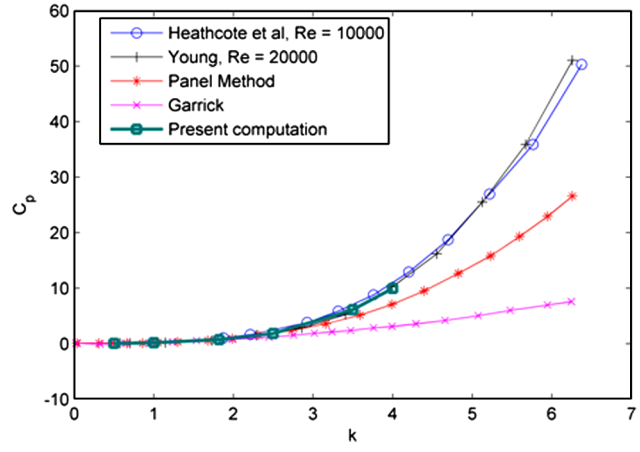

b) Power input coefficient

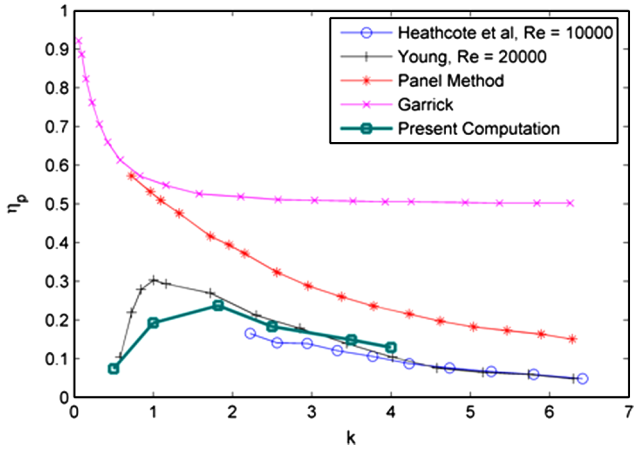

c) Propulsive efficiency

Fig. 4 Comparison of computed aerodynamic coefficients with available data (adapted from Heathcote et al. [22]).

IV. Results and Discussion on Free-Flight Computations

Prediction of aerodynamic forces and trajectories on a free-flapping wing is considered. Prior work by the present authors on rigid [11] and flexible wings [26] indicate that thrust is produced when there is a nonsymmetric motion of the wing and/or asymmetry between the leading and trailing edges. A more comprehensive analysis based on vortex dynamics is presented to understand the mechanics of thrust generation. An elliptical airfoil and a NACA airfoil of 12% thickness are considered as suitable cross section profiles for a wing of aspect ratio 2. Composite overlapping meshes are generated surrounding the wing as shown in Fig. 1. The ratio of the density of the wing to that of the surrounding fluid is assumed to be 10. A higher value is chosen deliberately so that the wing travels with a lower speed in the specified computational domain. A rotational motion of the form $\theta_i = -\theta_0(1 - \cos 2\pi f t)$ is specified about a coordinate axis i as explained in Fig. 6. Using these kinematics, three different modes of rotation are investigated to study the effect of independent and coupled rotations on forward flight at a reduced frequency $k = 1.43$, Strouhal number $St = 0.49$, and Reynolds number $Re = 329$.

For independent rotations, the wing is rotated only about a single axis (X or Z axes) whereas, for coupled rotations, at least two simultaneous rotations (X and Z axes) are performed. At all times $t \geq 0$, the wing flaps with no incoming freestream and the aerodynamic forces are integrated to obtain the position of the wing. For all cases considered here, the wing is constrained to move along the X axis and the solutions are computed until the wing reaches the boundary of the inner Cartesian grid (inner cube in Fig. 2). A comparison of the thrust coefficients for the elliptical case and NACA 0012 wing for rotations about different axes are shown in Figs. 7a, 7c, and 7e and the corresponding trajectories in Figs. 7b, 7d, and 7f. For rotation about the X or Z axes as in Figs. 7a–7d, it is observed that the thrust coefficients are higher for the NACA 0012 wing when compared with the elliptical cross section wing and, hence, the NACA 0012 wing accelerates faster than the elliptical cross section wing. This clearly indicates that asymmetry between the leading and trailing edge of the wing plays a significant role in thrust generation. For simultaneous rotation about the X and Z axes as in Figs. 7e and 7f, it is observed that both the NACA 0012 wing and the elliptical cross section wing produce similar characteristics and they accelerate with almost the same speed. Comparing Figs. 7e and 7a we can also infer that the simultaneous rotation mode produces

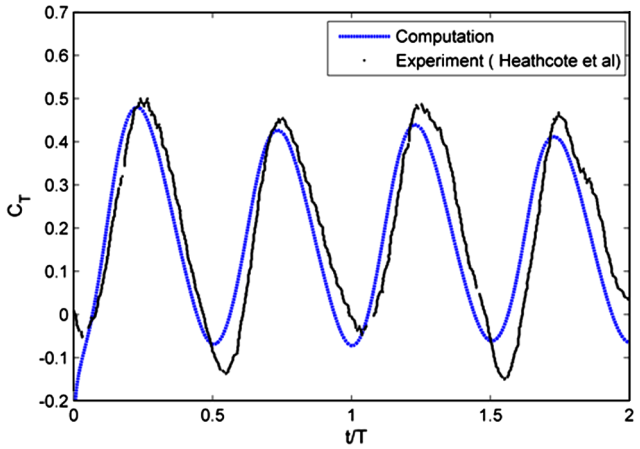

Fig. 5 Comparison of computed thrust coefficients with experiments from Heathcote et al. [22].

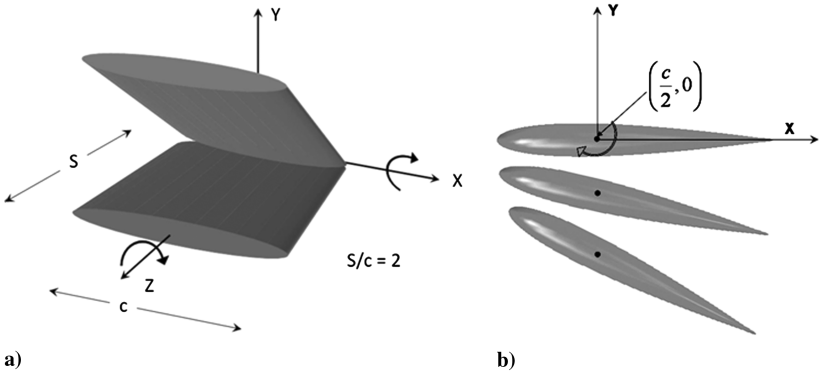

Fig. 6 Wing kinematics about various coordinate axes.

larger amounts of thrust compared with rotation about a single axis. This draws us to the conclusion that thrust can be generated through proper 1) geometric asymmetry (i.e., when there is asymmetry between the leading and trailing edges of the wing), and 2) coupled kinematics (i.e., when there is a coupled symmetric motion of the wing). For both these cases, the vortex shedding patterns are investigated. Figures 8 and 9 show the Z-vorticity component for the NACA 0012 wing and the elliptical cross- section wing, respectively. Two different time instances are considered corresponding to when the wing is at the start of the as cycle as in Figs. 8a, 8c, 8e, 9a, 9c, and 9e and when it has completed half-cycle as in Figs. 8b, 8d, 8f, 9b, 9d, and 9f. When there is a rotational motion either about the X or Z axes, the vortex structures generated from the trailing edge are symmetric with respect to that generated at the leading edge for an elliptical cross section wing, whereas they are asymmetric for the NACA 0012 wing. However, for the coupled rotation mode, both types of wings produce asymmetric vortex structures. Hence, it can be concluded that the presence of geometrical asymmetry and/or coupled kinematics can influence the structure of the shed vortices leading to thrust generation. Based on vortex dynamics, it is now explained as to how this vortex asymmetry leads to thrust generation. As mentioned earlier, the theory developed by Wu [12] is used to express the net aerodynamic force acting on a solid body as a function of vorticity moments and inertial forces. Consider a region R_f occupied by an infinite viscous fluid bounded by R_∞ as shown in Fig. 10 and assume that the solid body occupies a region R_b.

According to Wu [12], the aerodynamic force acting on a three-dimensional object is given by

$$F = -\frac{1}{2}\frac{\mathrm{d}\alpha}{\mathrm{d}t} + \rho_f \frac{\mathrm{d}}{\mathrm{d}t}\int_{R_b} u(r',t)\,\mathrm{d}R \tag{15}$$

where $\boldsymbol{u}$ is the velocity of the solid body and α, the first moment of vorticity, given by

$$\alpha = \int_{R_\infty} r' \times \varpi \mathrm{d}R \tag{16}$$

Because the focus is on understanding thrust generation, only the first component of Eqs. (15) and (16) is considered. Moreover, only the Z component of vorticity is taken because the wing flaps in the X-Y plane. This reduces Eq. (16) to

$$\alpha = \int_{R_\infty} y\varpi_Z \,\mathrm{d}R \tag{17}$$

During each half-stroke, both positive and negative vortices are shed from the wing. Based on this fact, the vorticity moment in Eq. (17) is split into a sum of positive and negative vorticity moments as follows:

$$\alpha = \int_{R_p} y|\varpi_{zp}|\mathrm{d}R - \int_{R_n} y|\varpi_{zn}|\mathrm{d}R = \alpha_p - \alpha_n \tag{18}$$

where R_p and R_n denote regions of positive (ϖ_p) and negative (ϖ_n) vorticity, respectively. To make sense of Eq. (18), the quantities y_{vp} and y_{vn}, which are the ordinates of the geometric center of the region R_p and R_n weighted by the vorticity, are defined as follows:

$$y_{pv} = \frac{\int_{R_p} y|\varpi_{zp}|\mathrm{d}R}{\int_{R_p}|\varpi_{zp}|\mathrm{d}R}, \qquad y_{nv} = \frac{\int_{R_n} y|\varpi_{zn}|\mathrm{d}R}{\int_{R_n}|\varpi_{zn}|\mathrm{d}R} \tag{19}$$

Differentiating Eq. (19) once with respect to time and using Eq. (18), it can be shown that the rate of change of the first moment of positive/negative vorticity

$$\frac{\mathrm{d}\alpha_{p/n}}{\mathrm{d}t}$$

is related to the velocity of the positive and negative vortices as follows:

$$\begin{aligned}\dot{\alpha}_p &= \dot{y}_{pv}\int_{R_p}|\varpi_{zp}|\mathrm{d}R + y_{pv}\frac{\mathrm{d}}{\mathrm{d}t}\int_{R_p}|\varpi_{zp}|\mathrm{d}R\\ \dot{\alpha}_n &= \dot{y}_{nv}\int_{R_n}|\varpi_{zn}|\mathrm{d}R + y_{nv}\frac{\mathrm{d}}{\mathrm{d}t}\int_{R_n}|\varpi_{zn}|\mathrm{d}R\end{aligned} \tag{20}$$

Using the principle of conservation of total vorticity in R_∞, it can be shown that

$$\int_{R_p}|\varpi_p|\mathrm{d}R = \int_{R_n}|\varpi_n|\mathrm{d}R \tag{21}$$

Equation (21) is verified numerically for both the elliptical cross section wing and the NACA 0012 wing for all computational cases considered in this paper. Figures 11a and 11b show the total normalized positive and negative vorticity computed in the inner cube grid during one cycle of oscillation for rotation about (X), (Z), and (X and Z) axes. The agreement with Eq. (21) is excellent with the maximum deviation estimated to be 0.56 %. Using Eqs. (20) and (21) in Eq. (15), the horizontal force acting on the body is given by

$$\begin{aligned}F_1 = -\frac{1}{2}\rho_f\left[(\dot{y}_p - \dot{y}_n)\int_{R_p}|\varpi_{zp}|\mathrm{d}R + (y_p - y_n)\frac{\mathrm{d}}{\mathrm{d}t}\int_{R_p}|\varpi_{zp}|\mathrm{d}R\right]\\ + \rho_f\frac{\mathrm{d}}{\mathrm{d}t}\int_{R_b}u(r,t)\mathrm{d}R = -\frac{1}{2}\rho_f Q_v + \rho_f\frac{\mathrm{d}}{\mathrm{d}t}\int_{R_b}u(r,t)\,\mathrm{d}R\end{aligned} \tag{22}$$

In Eq. (22), the first term Q_v represents the relative rate at which the vortices are convected away from the wing and the second term represents the inertial contribution of the displaced fluid. During the initial stages of flapping when there is hardly any horizontal motion, there is no horizontal component of the inertial term and hence, thrust generation purely depends on the relative contribution of positive and negative vorticity convection rates. It can be seen that thrust is produced if $Q_v > 0$, that is, when positive vorticity moves away from the wing at a faster rate than negative vorticity. To verify this, the

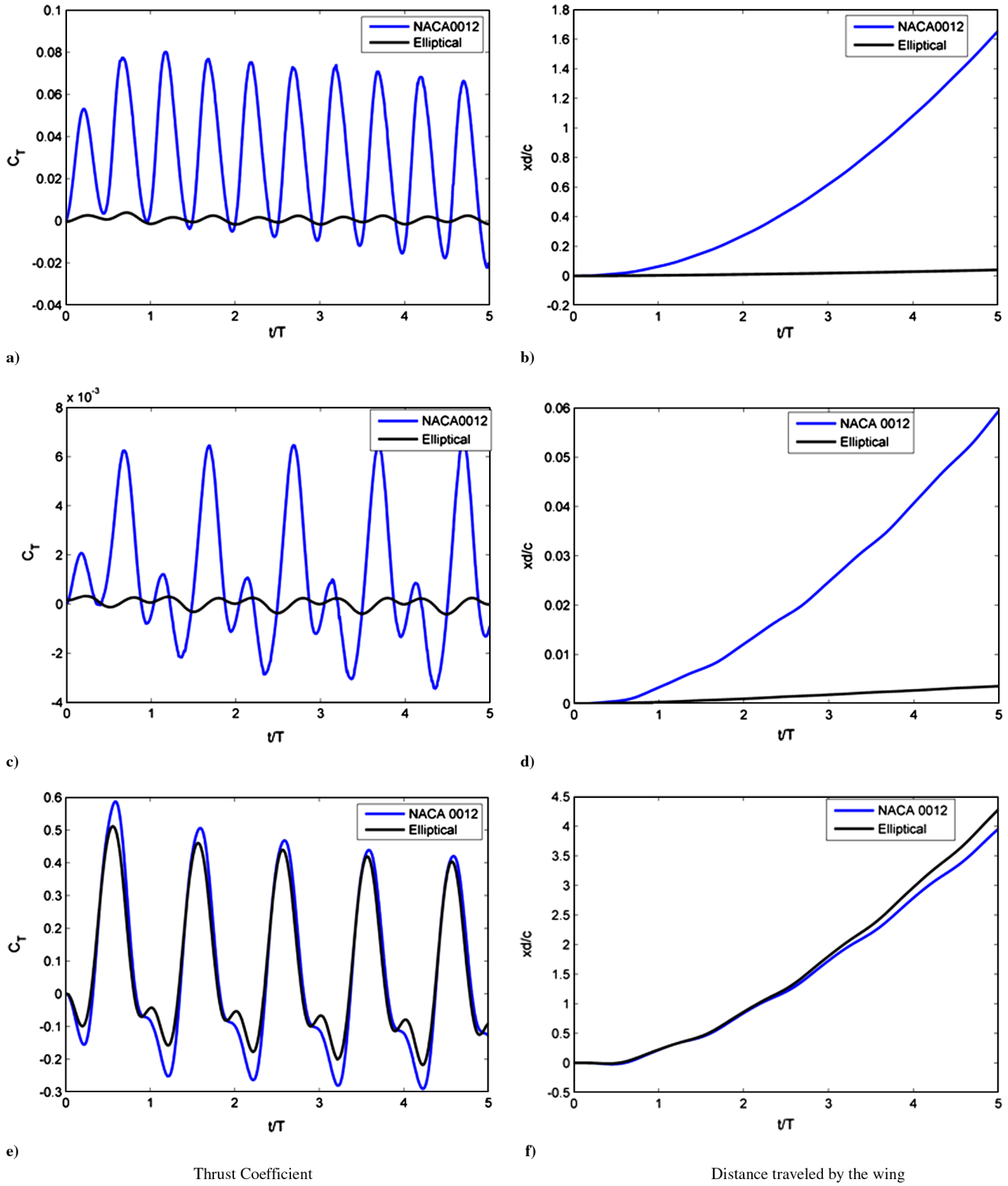

Fig. 7 Comparison of computed thrust coefficients and trajectories for a NACA 0012 wing with an elliptical cross section wing for flapping about a–b) *X* axis, c–d) *Z* axis, and e–f) *X*and *Z* axes.

variation of Q_v over one cycle of oscillation and its corresponding mean value are plotted for both the elliptical cross section wing and the NACA 0012 wing for rotations about various axes.

For rotation about *X* axis (Fig. 12a), it can be seen that the mean value of Q_v for the NACA 0012 wing over one cycle of oscillation is greater than that for the elliptical cross section wing. Thrust is generated as a result of geometric asymmetry. A similar situation occurs for rotation about *Z* axis (Fig. 12b). However, Q_v is found to be 2 orders of magnitude smaller than the previous case. This is because both positive and negative vortices are convected away from the wing at almost the same rate. For simultaneous rotation about *X* and *Z* axes (Fig. 12c), the level of asymmetry created in the vortical structures are similar for the elliptical cross section wing and the NACA 0012 wing, with the elliptical cross section wing having a higher relative vorticity convection rate than the NACA 0012 wing. The thrust generated by the elliptical cross section wing is higher than that generated by the NACA 0012 wing, and as a result, the former travels faster than the latter (Figs. 7e and 7f).

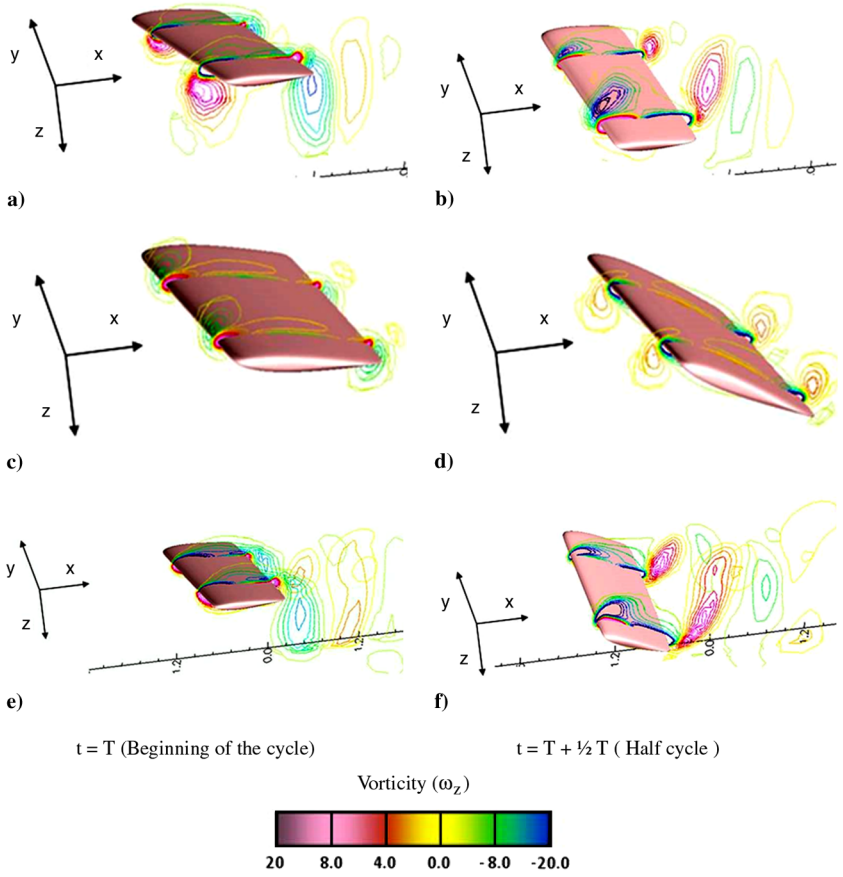

Fig. 8 Computed vorticity contours at the beginning of the cycle ($t = T$) and at half-cycle ($t = T + 1/2T$) for a flapping NACA 0012 cross section wing for rotation about a–b) X axis, c–d) Z axis, and e–f) X and Z axes (T being the period of one oscillation).

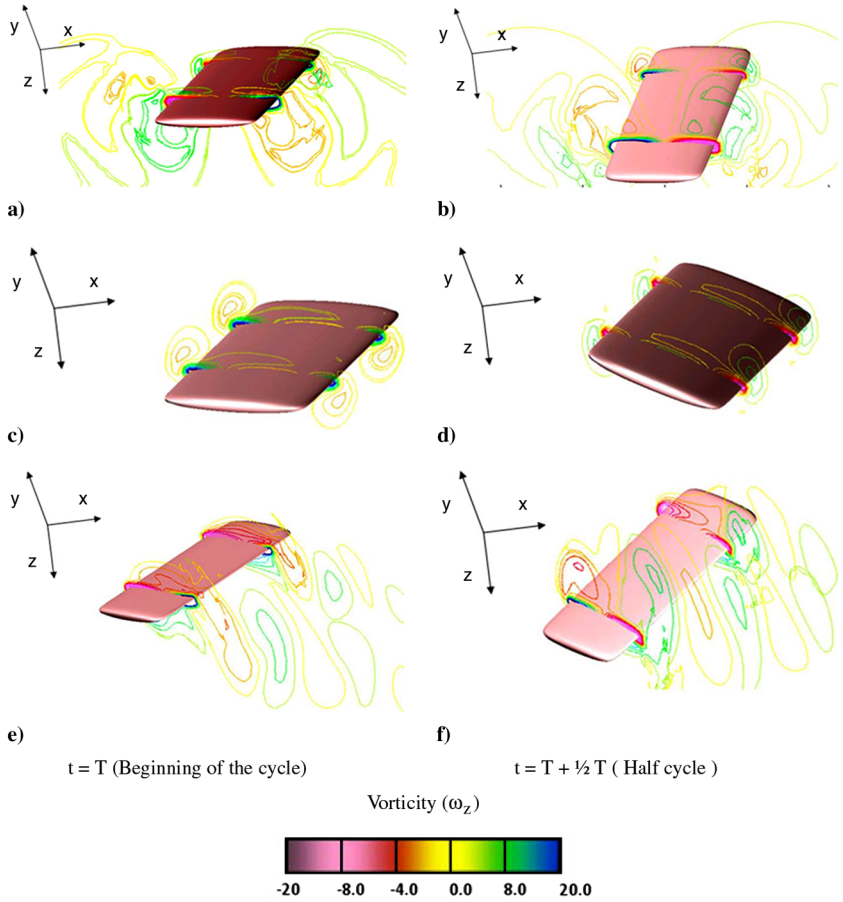

Fig. 9 Computed vorticity contours at the beginning of the cycle ($t = T$) and at half-cycle ($t = T + 1/2T$) for a flapping elliptical cross section wing for rotation about a–b) X axis, c–d) Z axis, and e–f) X and Z axes (T being the period of one oscillation).

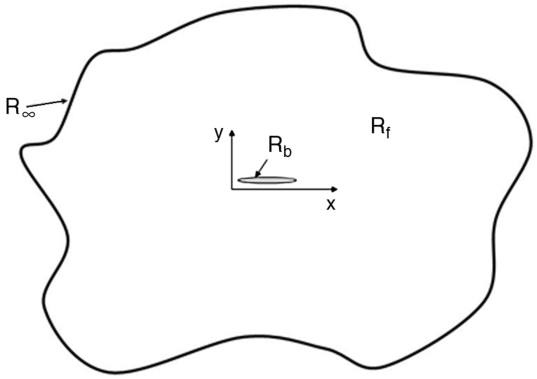

Fig. 10 Illustration of the region occupied by the wing and the fluid bounded at infinity.

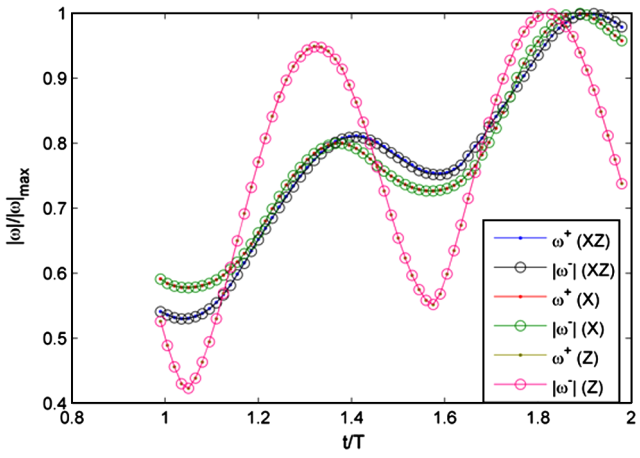

a) Wing with NACA 0012 cross-section

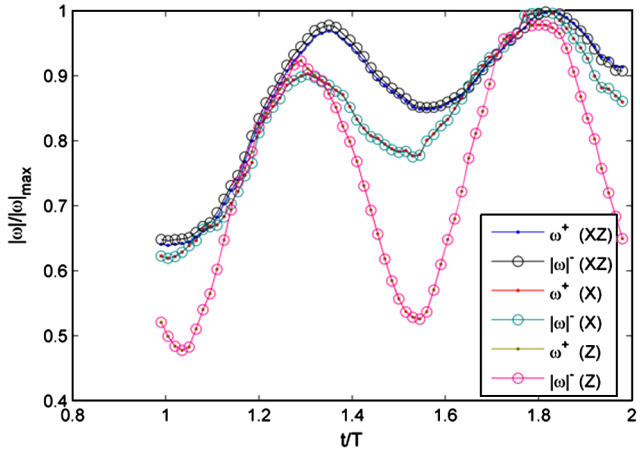

b) Wing with elliptical cross-section

Fig. 11 Computed variation of normalized positive and negative vorticity with time for rotation about different axes.

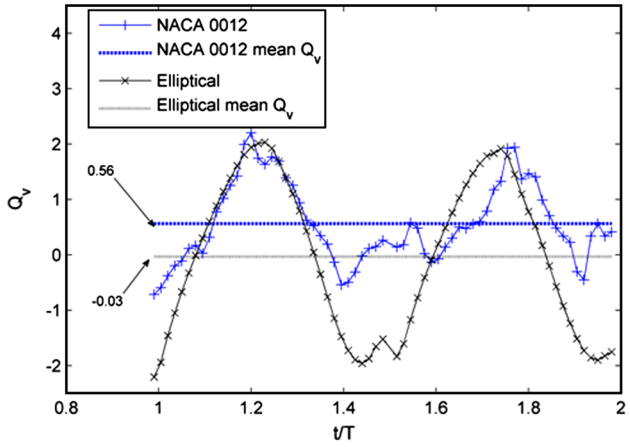

a) Rotation about x-axis

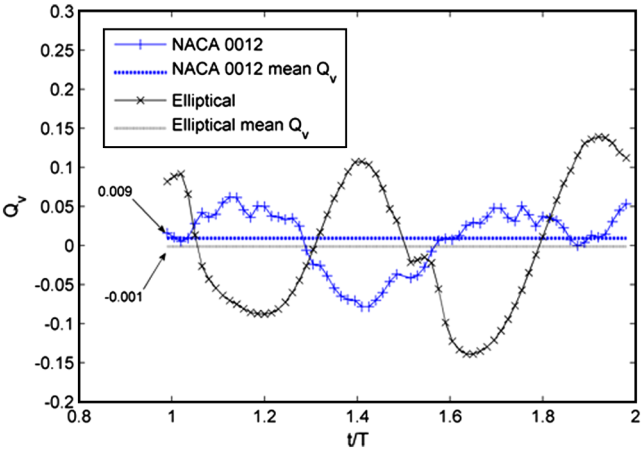

b) Rotation about z-axis

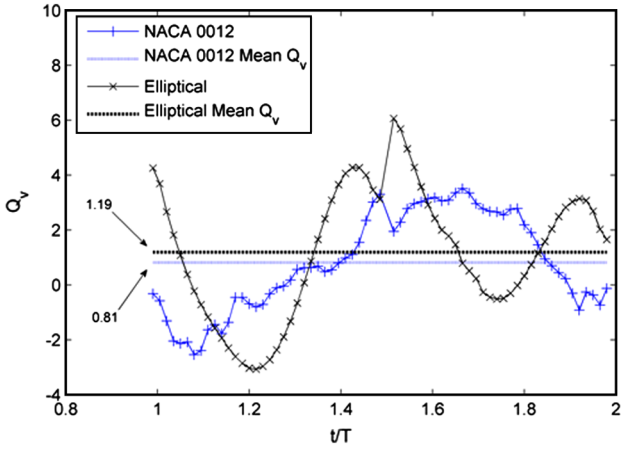

c) Rotation about x- and z-axes

Fig. 12 Computed variation of Q_v over one cycle for rotation about different axes for the NACA 0012 cross section wing and the elliptical cross section wing.

V. Conclusions

Numerical solutions were computed for the flow past flapping wings using the unsteady incompressible Navier–Stokes solver cgins. Using available experimental and computational data, the code is validated for the case of a plunging NACA 0012 cross section wing and reasonable comparisons were obtained. The major aspect that was discussed in the present paper was the free flight of a flapping wing. Rotational motions about different axes were considered and the aerodynamic characteristics were computed for a NACA 0012 cross section wing as well as an elliptical cross section wing. The key aspect that differentiated these two types of wings and the various rotational motions was the manner in which vortices were convected away from the wing surface. Using a nonconventional approach to model the forces acting on a wing, it was shown that the relative convection rates of positive and negative vorticity play an important role in thrust generation. Using this approach, it was explained why coupled rotation modes or asymmetry between leading and trailing edges is beneficial to thrust. This approach can easily be applied to analyze thrust generation in flexible airfoils/wings.

Acknowledgment

The authors would like to thank William D. Henshaw and the rest of Overture team at the Center for Applied Scientific Computing,

Lawrence Livermore National Laboratory, University of California for their valuable suggestions and comments and permissions to use and modify the composite grid incompressible Navier–Stokes and Overture code.

References

[1] Jones, K. D., Dohring, C. M., and Platzer, M. F., "Experimental and Computational Investigation of the KnollerBetz Effect," *AIAA Journal*, Vol. 36, No. 7, 1998, pp. 1240–1246. doi:10.2514/2.505

[2] Wang, Z. J., Birch, J. M., and Dickinson, M. H., "Unsteady Forces and Flows in Low Reynolds Number Hovering Flight: Two-Dimensional Computations vs Robotic Wing Experiments," *The Journal of Experimental Biology*, Vol. 207, No. 3, Jan. 2004, pp. 449–460. doi:10.1242/jeb.00739

[3] Ramamurti, R., and Sandberg, W. C., "A Three-Dimensional Computational Study of the Aerodynamic Mechanisms of Insect Flight," *The Journal of Experimental Biology*, Vol. 205, No. 10, 2002, pp. 1507–1518.

[4] Tuncer, I. H., and Platzer, M. F., "Thrust Generation Due to Airfoil Flapping," *AIAA Journal*, Vol. 34, No. 2, 1996, pp. 324–331. doi:10.2514/3.13067

[5] Freymuth, P., "*Propulsive Vortical Signature of Plunging and Pitching Airfoils*, *AIAA Journal*, Vol. 26, No. 7, 1988, pp. 881–883. doi:10.2514/3.9982

[6] Anderson, J. M., Streitlien, K., Barret, D. S., and Triantafyllou, M. S., "Oscillating Foils of High Propulsive Efficiency," *Journal of Fluid Mechanics*, Vol. 360, 1998, pp. 41–72. doi:10.1017/S0022112097008392

[7] Vandenberghe, N., Zhang, J., and Childress, S., "Symmetry-Breaking Leads to Forward Flapping Flight," *Journal of Fluid Mechanics*, Vol. 506, 2004, pp. 147–155. doi:10.1017/S0022112004008468

[8] Alben, S., and Shelly, M., "Coherent Locomotion as an Attracting State for a Free Flapping Body," *Proceedings of the National Academy of Sciences of the United States of America*, Vol. 102, No. 32, 2005, pp. 11163–11166. doi:10.1073/pnas.0505064102

[9] Beal, D. N., Hover, F. S., Triantafyllou, M. S., Liao, J. C., and Lauder, G. V., "Passive Propulsion in Vortex Wakes," *Journal of Fluid Mechanics*, Vol. 549, 2006, pp. 385–402. doi:10.1017/S0022112005007925

[10] Lai, J. C. S., and Platzer, M. F., "Characteristics of a Plunging Airfoil at Zero Freestream Velocity," *AIAA Journal*, Vol. 39, No. 3, 2001, pp. 531–534. doi:10.2514/2.1340

[11] Chandar, D., and Damodaran, M., "Computational Study of Unsteady Low Reynolds Number Airfoil Aerodynamics Using Moving Overlapping Meshes," *AIAA Journal*, Vol. 46, No. 2, 2008, pp. 429–438. doi:10.2514/1.31499

[12] Wu, J. C., "Theory for Aerodynamic Force and Moment in Viscous Flows," *AIAA Journal*, Vol. 19, No. 4, 1981, pp. 432–441. doi:10.2514/3.50966

[13] Miller, L. A., and Peskin, C. S., "When Vortices Stick: An Aerodynamic Transition in Tiny Insect Flight," *The Journal of Experimental Biology*, Vol. 207, No. 17, 2004, pp. 3073–3088. doi:10.1242/jeb.01138

[14] Henshaw, W. D., "OverBlown/cgins: A Fluid Flow Solver for Overlapping Grids, Reference Guide, Version 1.0," Univ. of California Radiation Lab., Paper MA-134289, 2003, pp. 1–51.

[15] Brown, D. L., Chesshire, G. S., Henshaw, W. D., and Quinlan, D. J., "Overture: An Object Oriented Software System for Solving Partial Differential Equations in Serial and Parallel Environments," Eighth Conference on Parallel Processing for Scientific Computing, Society for Industrial and Applied Mathematics Paper CP97, 1997.

[16] Chesshire, G., and Henshaw, W. D., "Composite Overlapping Meshes for the Solution of Partial Differential Equations," *Journal of Computational Physics*, Vol. 90, No. 1, 1990, pp. 1–64. doi:10.1016/0021-9991(90)90196-8

[17] Henshaw, W. D., "Ogen: An Overlapping Grid Generator for Overture," UCRL MA-132237, 2003, pp. 1–78.

[18] Henshaw, W. D., "Mappings for Overture: A Description of the Mapping Class and Documentation for Many Useful Mappings," Univ. of California Radiation Lab., Paper MA-132239, 2003, pp. 1–284.

[19] Balay, S., Buschelman, K., Eijkhout, V., Gropp, W. D., Kaushik, D., Knepley, M. G., McInnes, L. C., Smith, B. F., and Zhang, H., "PETSc Users Manual," Revision 3.0.0, Argonne National Lab., 2008.

[20] Van der Vorst, H., "Bi-CGSTAB: A Fast and Smoothly Converging Variant of Bi-CG for the Solution of Non-Symmetric Linear Systems," *SIAM Journal on Scientific and Statistical Computing*, Vol. 13, No. 2, 1992, pp. 631–644. doi:10.1137/0913035

[21] Henshaw, W. D., and Schwendeman, D. W., "Moving Overlapping Grids with Adaptive Mesh Refinement for High-Speed Reactive and Non-Reactive Flow," *Journal of Computational Physics*, Vol. 216, No. 2, 2006, pp. 744–779. doi:10.1016/j.jcp.2006.01.005

[22] Heathcote, S., Wang, Z., and Gursul, I., "Effect of Spanwise Flexibility on Flapping Wing Propulsion," *Journal of Fluids and Structures*, Vol. 24, No. 2, 2008, pp. 183–199. doi:10.1016/j.jfluidstructs.2007.08.003

[23] Young, J., "Numerical Simulation of the Unsteady Aerodynamics of Flapping Airfoils," Ph.D. Dissertation, School of Aerospace, Civil, and Mechanical Engineering, New South Wales Univ., Canberra, Australia, 2005.

[24] Garrick, I. E., "Propulsion of a Flapping and Oscillating Airfoil," NACA Rept. 567, 1936, pp. 419–427.

[25] Ashraf, M. A., Lai, J. C. S., and Platzer, M. F., "Numerical Analysis of Flapping Wing Aerodynamics," *16th Australasian Fluid Mechanics Conference*, Univ. of Queensland, Queensland, Australia, Dec. 2007, pp. 1283–1290.

[26] Chandar, D., and Damodaran, M., "Computation of Low Reynolds Number Flexible Flapping Wing Aerodynamics Using Overlapping Grids," *47th AIAA Aerospace Sciences Meeting and Exhibit*, AIAA Paper 2009-1273, Orlando, FL, 2009.